Tectonics

Supporting Information for

A Middle Crustal Channel of Radial Anisotropy Beneath the Northeastern Basin and Range

Justin Wilgus[1], Chengxin Jiang[1*], Brandon Schmandt[1]

1. Department of Earth and Planetary Sciences, University of New Mexico, Albuquerque, NM, USA
*now at Research School of Earth Sciences, The Australian National University, Acton, ACT, Australia

Contents of this file

Introduction

The supplementary information provided here includes 10 figures and 2 tables. These materials expand on data coverage, processing, methodology, and results.

Figure S1. Interstation Rayleigh wave ray path coverage of study area.
Figure S2. Regional Love and Rayleigh wave phase velocity maps.
Figure S3. Observed and predicted Dispersion curves, and 1D BMMC inversion V_S and anisotropy results from 1-D grid point point 40.5°, -115.5°.
Figure S4. Chi-squared (χ^2) misfit maps.
Figure S5. Depth-integrated absolute value of crustal radial anisotropy maps.
Figure S6. BMMC inversion parameterization and constraint test results from 1-D grid point 40°, -116°.
Figure S7. Depth averaged isotropic V_S and radial anisotropy maps.
Figure S8. Isotropic V_S and anisotropy results from inversion case 4 without statistical culling.
Figure S9. Isotropic V_S and anisotropy results from inversion case 5 without statistical culling.
Figure S10. Isotropic V_S and anisotropy results from inversion case 5 with statistical culling.
Table S1. Summary of seismic networks used for this study.
Table S2. Rayleigh and Love wave errors.

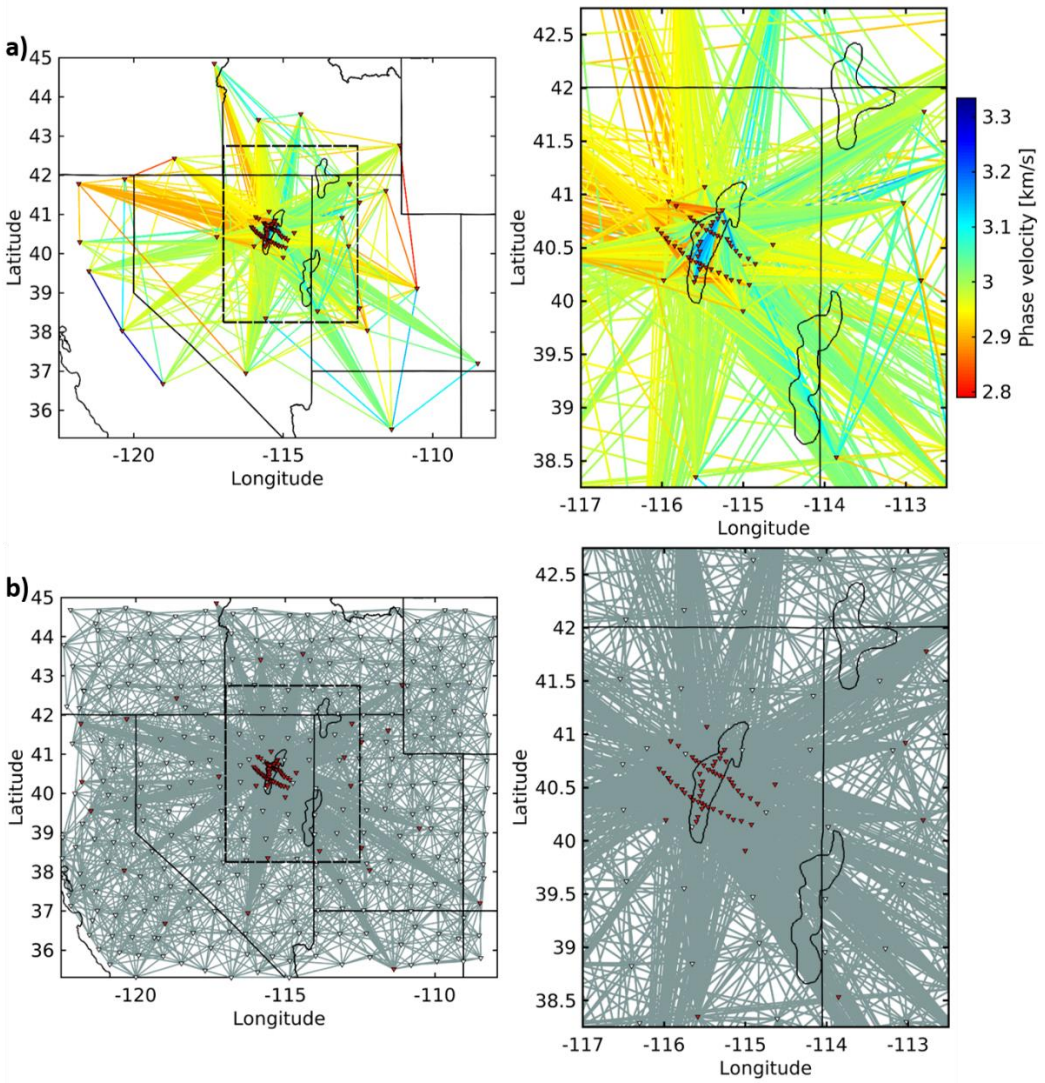

Figure S1. Interstation Rayleigh wave ray path coverage of study area retained for tomography at a 6 s period. (a) Left panel shows 1521 interstation Rayleigh wave phase velocity values calculated as a part of this study using RMSE and surrounding stations (red triangles; table 1) between 2010-2012. For Love waves 1631 interstation phase velocity values were contributed for 6 s period tomographic maps (Supplementary Information S2). Black dashes delineate study area enlarged in the right panel. Notice high density of interstation paths in the study region and high velocities that coincide with the location and strike of the RMCC. (b) Interstation Rayleigh wave phase velocity ray paths after combination with measurements from Ekström, (2017) made with TA stations between time period 2005-2008. Right panel again shows enlarged study area delineated with black dashed line in right panel. Notice increased regional path coverage and increased number of crossing paths within study region.

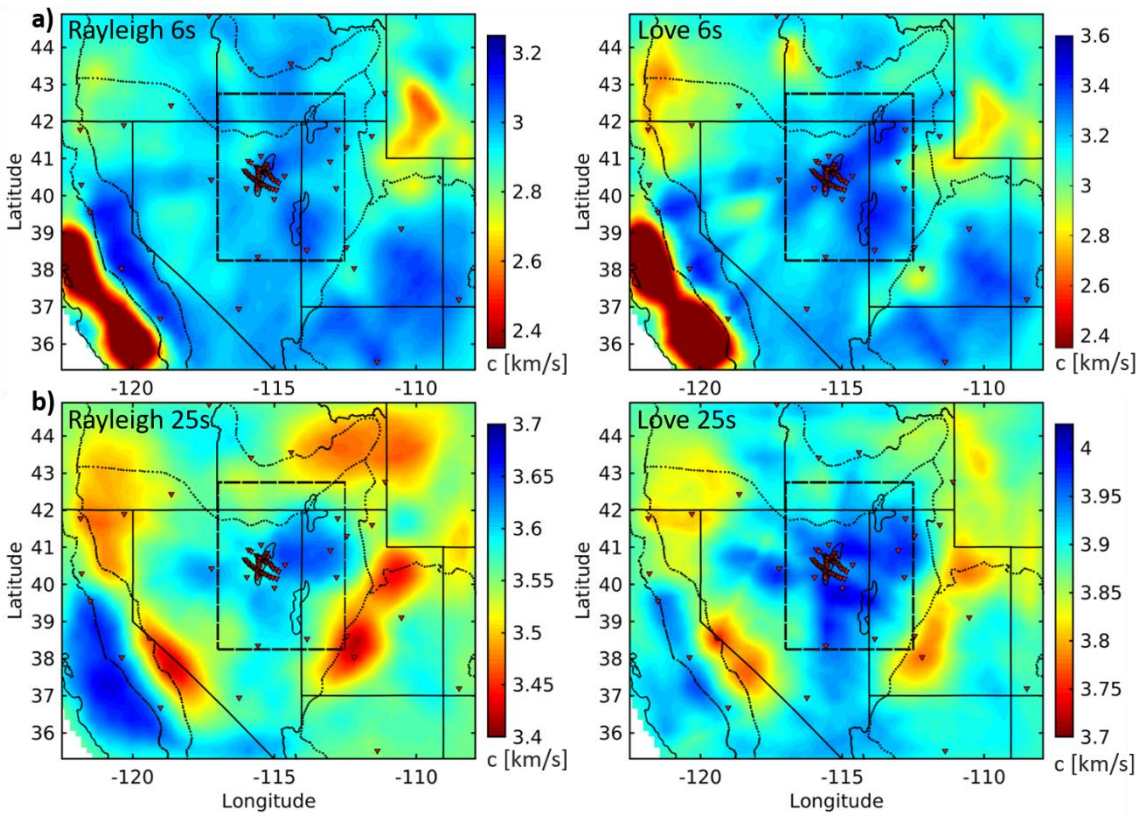

Figure S2. Regional Love and Rayleigh wave phase velocity maps. (a) 6 s period Rayleigh (left panel) and Love (right panel) wave phase velocity, c, maps. At a period of 6 s surface waves are sensitive to structures in the shallow crust. Mapped phase velocity anomalies agree with well-known geologic provinces such as the Colorado Plateau, San Joaquin valley, and the Sierra Nevada mountain range. Within the study region, particularly in Love wave maps, high velocity anomalies are coincident with the location of MCC's. (b) Same as (a) but for a period of 25 s which is sensitive to structures in the deep crust. The Basin and Range exhibits a fast phase velocity anomaly likely due to the shallow Moho allowing for sensitivity to high velocity mantle.

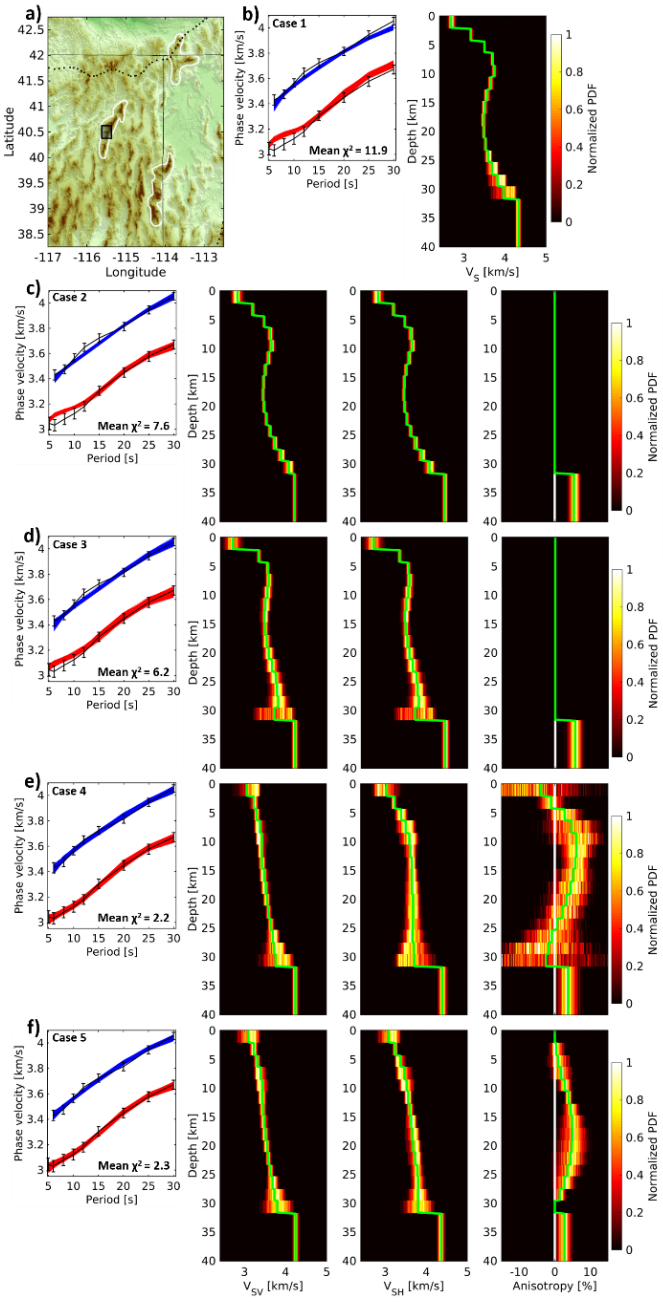

Figure S3. Observed and predicted dispersion curves and 1D BMMC inversion V_S and anisotropy results from 1-D grid point 40.5°, -115.5° centered on the southern portion of the RMCC. (a) Map showing the location of grid point area (black box). (b-f) Evolution of 1-D χ^2 dispersion misfits and V_S and anisotropy with depth for inversion cases 1-5. (b) Left panel shows observed (black lines) and predicted Love (blue lines) and Rayleigh (red lines) wave dispersion curves for inversion case 1 labeled in the upper left corner. Observation error bars are from Supplementary information table 2. Mean χ^2 dispersion misfits for each case are given in the left portion of each panel. Right panel shows the posterior probability distribution as a function of depth for V_S. Green line is the mean of the posterior distribution. (c) same as (b) but for inversion case 2 and right panels showing the posterior probability distribution as a function of depth for, V_{SV}, V_{SH}, and anisotropy. (d) same as (c) but for inversion case 3. Predicted curves for inversion cases 1-3 (b-d) do not fit observed curves well. (e) same as (f) but for inversion case 4. Notice decrease in χ^2 misfit and increase in width of 1 sigma corridor for, V_{SV}, V_{SH}, and anisotropy. (f) same as (e) but for inversion case 5. Inversion cases 4 and 5 (e, f) achieve similarly low χ^2 misfits.

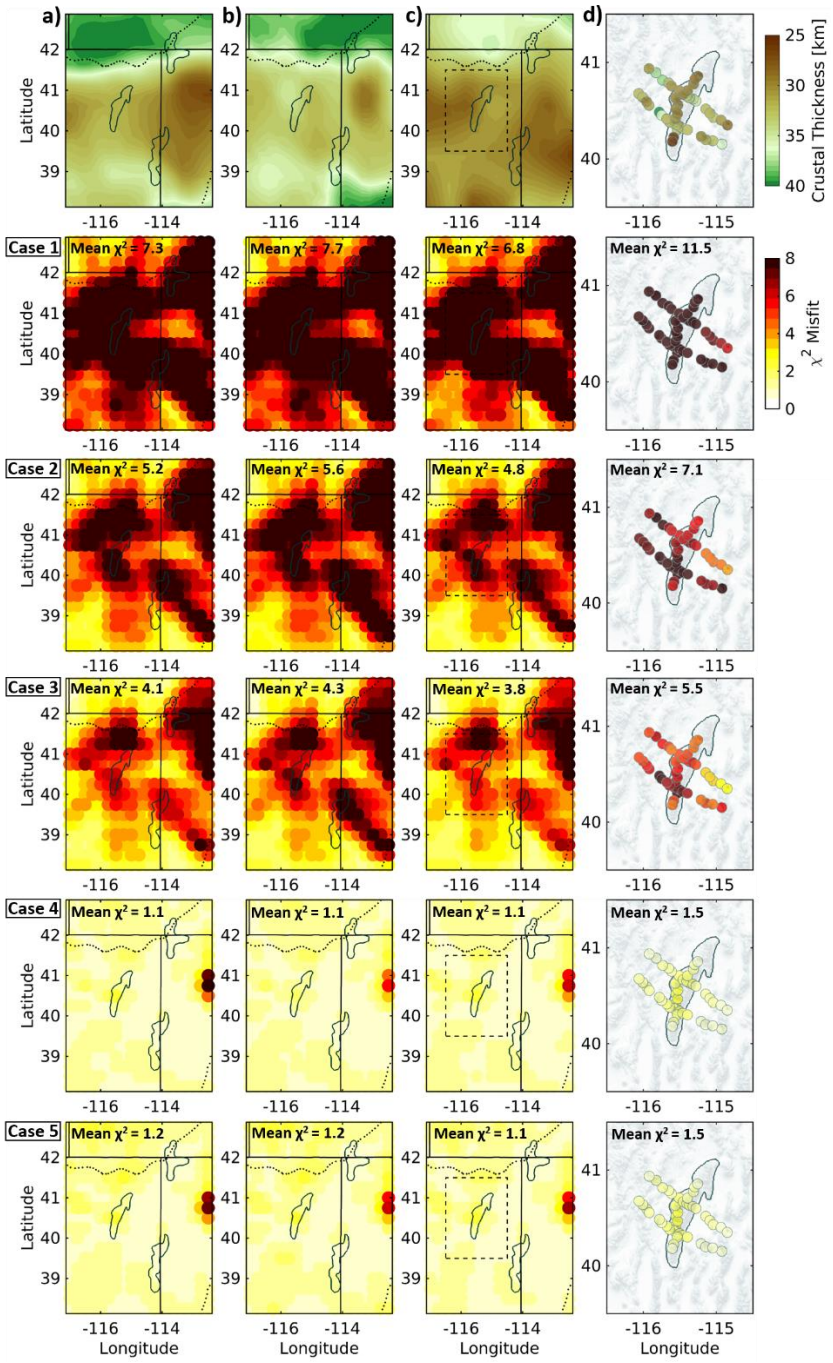

Figure S4. Chi-squared (χ^2) misfit maps of the study region for the five parameterization cases (described in section 3.3) and four different crustal thickness models. a) Top panel shows crustal thickness model of Schmandt et al., (2015). Following panels below top panel show χ^2 misfit map results when using crustal thickness in (a) as input to the BMMC inversion for cases 1-5, as labeled. Mean χ^2 misfits of the map area are given in the upper left portion of each map. Misfit map results in (a) are the same as what is shown in figure 4 but are shown again here for comparison. (b, c) Same as (a) but for the crustal thickness model of Shen et al., (2016), Buehler and Shearer, (2017), respectively. (d) Similar to (a-c) but local crustal thickness from Litherland and Klemperer, (2017) are only available beneath stations from the RMSE array. Dashed lines in (c) demarcate the area shown in (d). Inversion cases 4 and 5 achieve similarly low χ^2 misfits across all crustal thickness model inputs. Distribution and magnitude of χ^2 misfit are similar regardless of the choice of crustal thickness model.

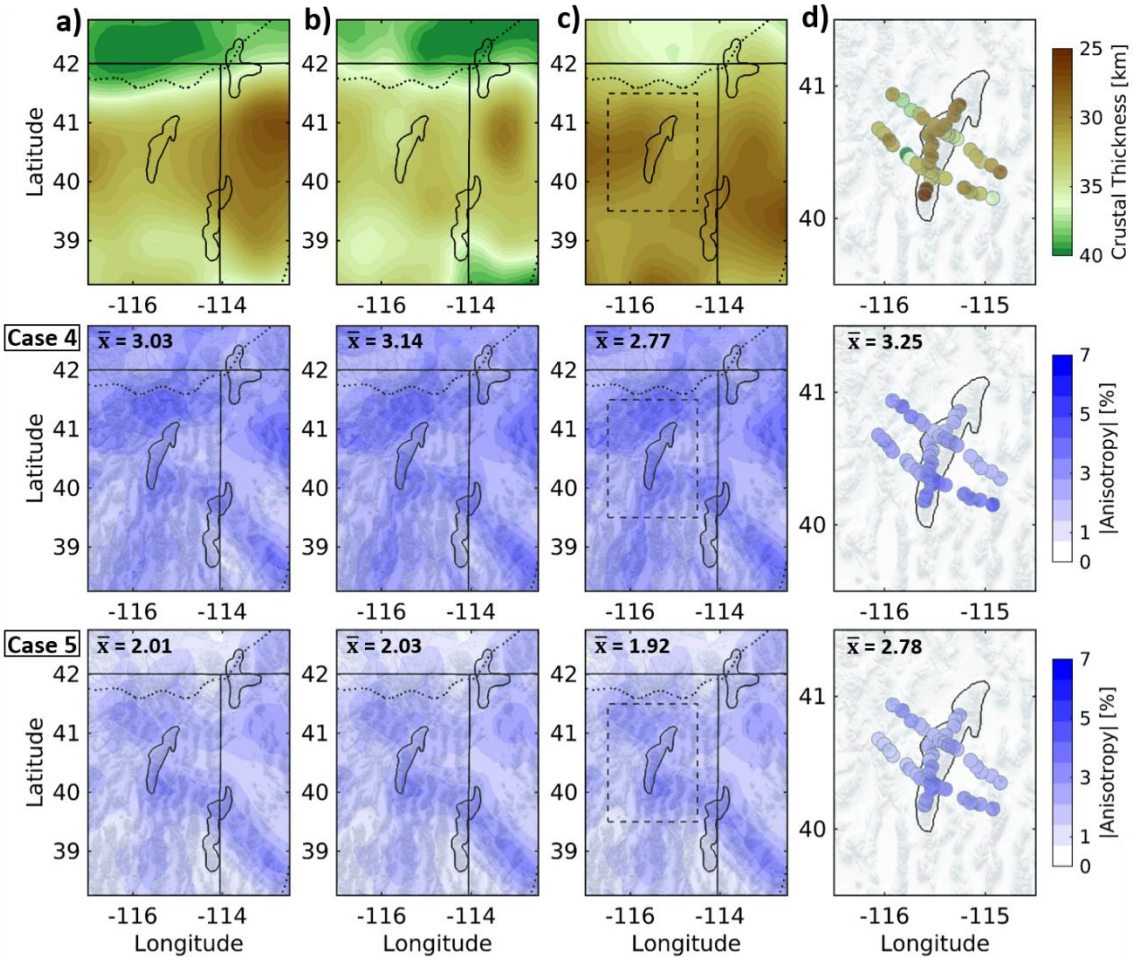

Figure S5. Same as figure 6 but including depth-integrated absolute value of crustal radial anisotropy from inversion cases 4 (also shown in fig 6) and 5 for comparison. a) The top panel shows the crust thickness model of Schmandt et al., (2015) and panels below top panel show depth-integrated absolute value of radial anisotropy when using crustal thickness in (a) as input to the BMMC inversion for inversion cases 4 (center) and 5 (bottom). Mean radial anisotropy of the map area ($\bar{x}$) is given in the upper left portion of each map. (b,c) Similar to (a) but showing results using the crustal thickness models of Buehler and Shearer, (2017) and (c) Shen and Ritzwoller, (2016), respectively. (d) Similar to a-c except local crustal thickness results from Litherland and Klemperer, (2017) are only available beneath stations from the RMSE array. Dashed lines in (c) demarcate the area shown in (d). Although the distribution of depth-integrated absolute value of crustal radial anisotropy are similar between inversion cases 4 and 5 there is a reduced magnitude of anisotropy in inversion case 5 relative to inversion case 4.

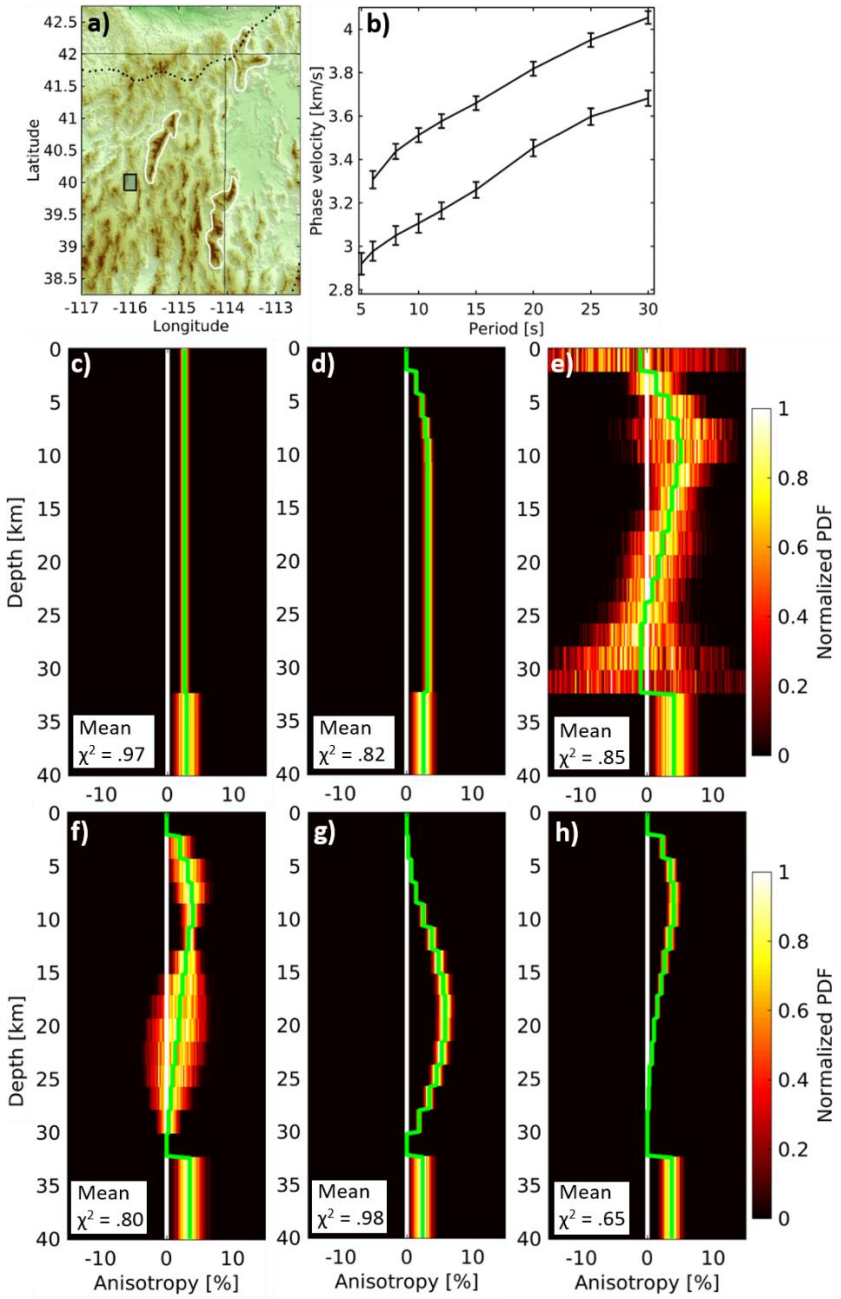

Figure S6. Effects of varying BMMC inversion parameterizations on posterior probability distribution of radial anisotropy as a function of depth from 1-D grid point 40°, -116°, the same grid point used by Moschetti et al., 2010a. (a) Map showing the location of grid point area (black box) and (b) associated dispersion curves and errors. Green lines are the mean of the posterior distribution. Mean χ^2 misfits for each case are given in the left portion of each panel. (c) Forced velocity increase with increasing depth, and an assumption of uniform radial anisotropy through the entire crust (similar to Xie et al., 2015). (d) Forced isotropy in the upper crust, forced increase in velocity with increasing depth, and equalized anisotropy in the middle and lower crust (similar to Moschetti et al., 2010a). (e) Parameterizations from inversion case 4. (f) Parameterizations from inversion case 5. (g) Allowing only b-spline 3 to be anisotropic in the crust. (h) Allowing only b-spline 2 to be anisotropic in the crust. The half-space mantle parameter is allowed to be anisotropic and this parameter is consistent throughout all of the inversion cases. All cases use the crustal thickness model of Schmandt et al., (2015).

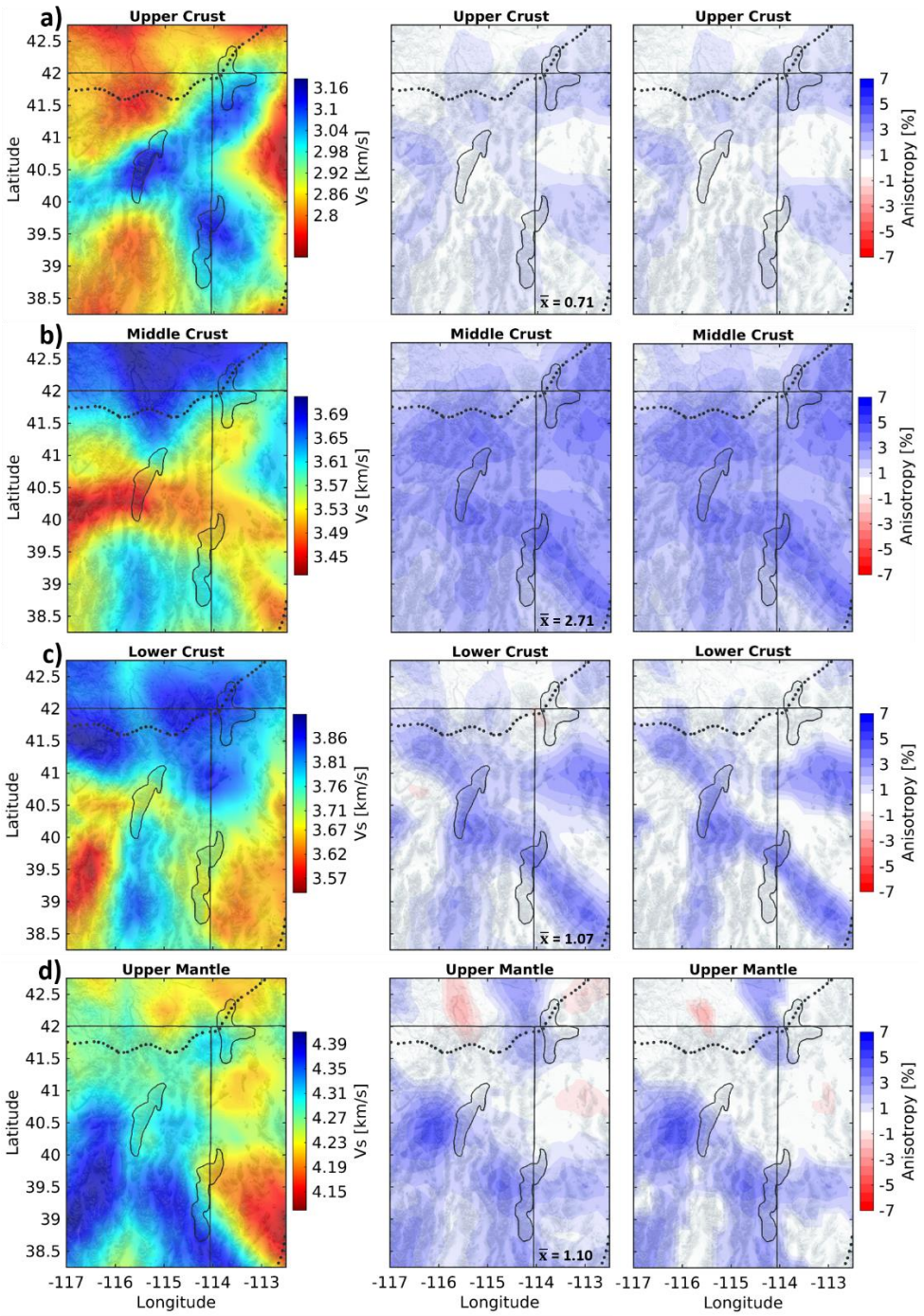

Figure S7. Same as Fig. 7 but for inversion case 5. Depth averaged isotropic V_S and radial anisotropy maps for the upper crust, middle crust, lower crust, and upper mantle. (a) Depth averaged isotropic V_S and radial anisotropy of the upper crust. Left panel shows isotropic velocity. Middle panel shows radial anisotropy results. The mean radial anisotropy of the map area ($\bar{x}$) is given in the lower right corner. Right panel shows only reliable results that have an absolute value of radial anisotropy greater than one standard deviation of the posterior. The upper crust maps average results between 0 and 5 km while the extent of depth averaging of the middle and lower crust is determined by evenly splitting the remaining thickness between 5 km and the Moho at each inversion point. (b-d) Same as (a) but for the middle and lower crust and upper mantle, respectively. All results shown in this figure are from inversion case 5 and correspond to inversions assuming the regional crust thickness model of Schmandt et al., (2015).

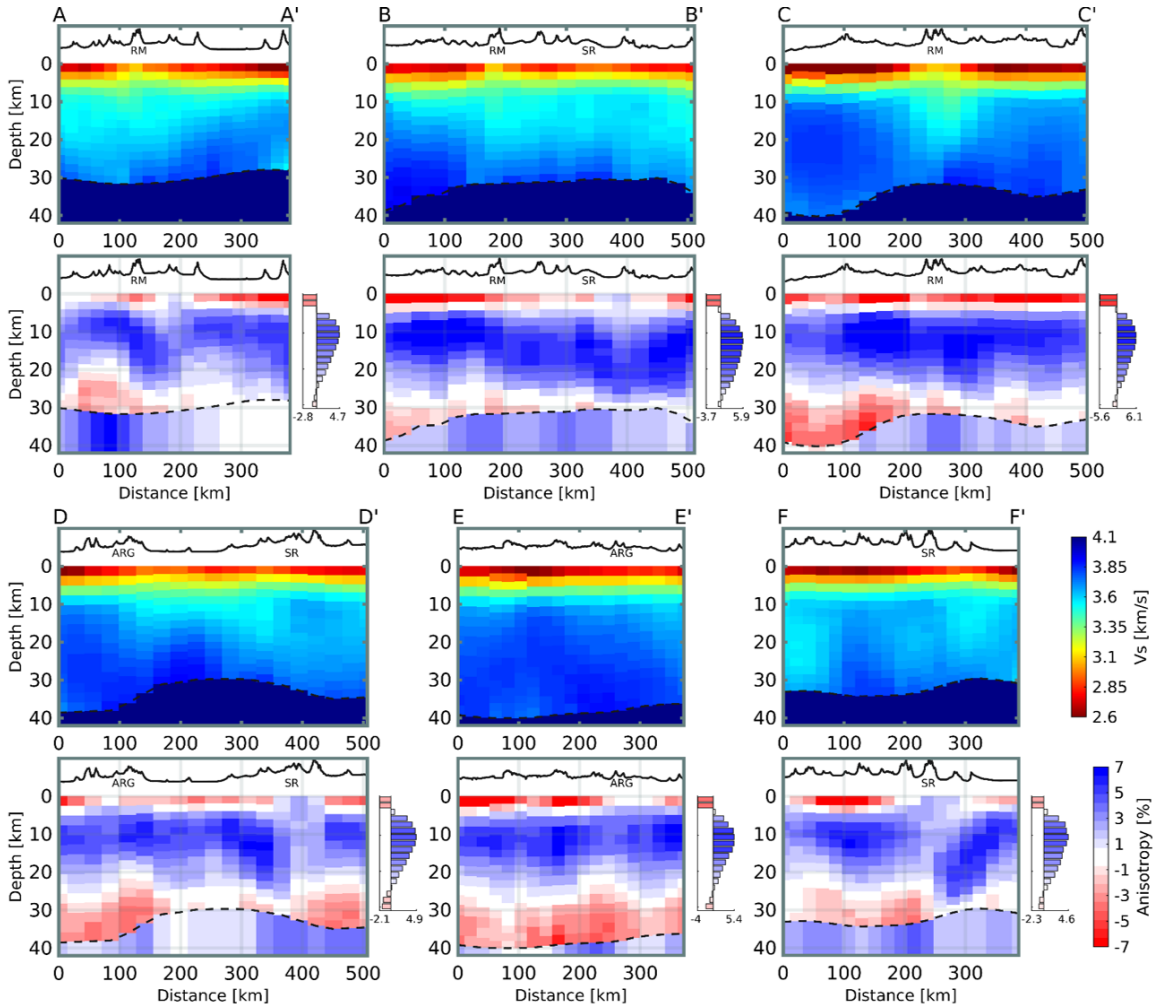

Figure S8. Same as figure 8, but showing isotropic V_S and anisotropy cross sectional (see figure 1) results from inversion case 4 without any statistical culling. Bar charts right of anisotropy cross-sections show average anisotropy profiles with depth for each cross-section. Anisotropy minima and maxima are labeled on the x-axis of each profile and colors correspond to anisotropy color bar. All panels shown here use the crustal thickness (dashed line) model of Schmandt et al., (2015). Topography is exaggerated 3 times in the profiles at the top of each panel.

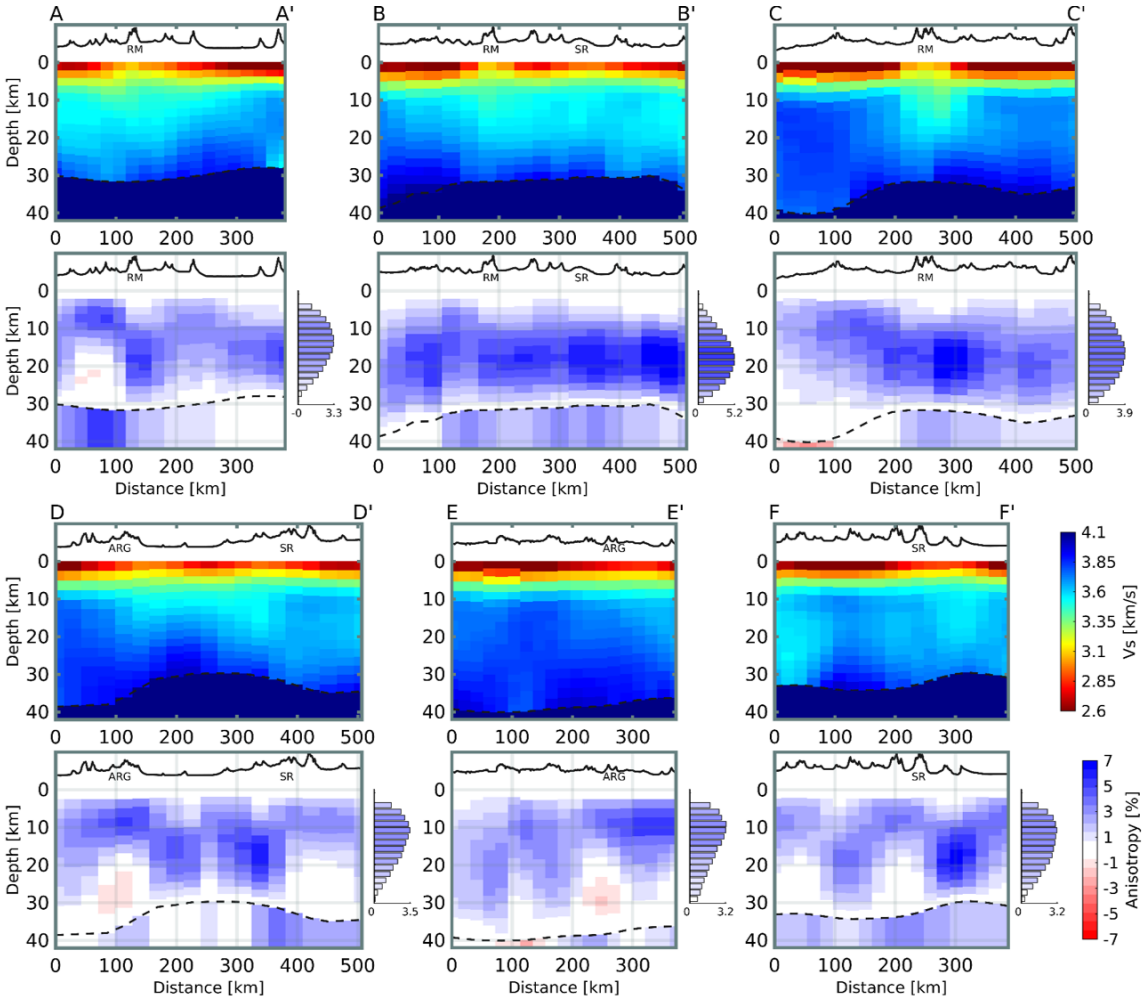

Figure S9. Same as figure 8, but showing isotropic V_S and anisotropy cross sectional (see figure 1) results from inversion case 5 without any statistical culling. Bar charts right of anisotropy cross-sections show average anisotropy profiles with depth for each cross-section. Anisotropy minima and maxima are labeled on the x-axis of each profile and colors correspond to anisotropy color bar. All panels shown here use the crustal thickness (dashed line) model of Schmandt et al., (2015). Topography is exaggerated 3 times in the profiles at the top of each panel.

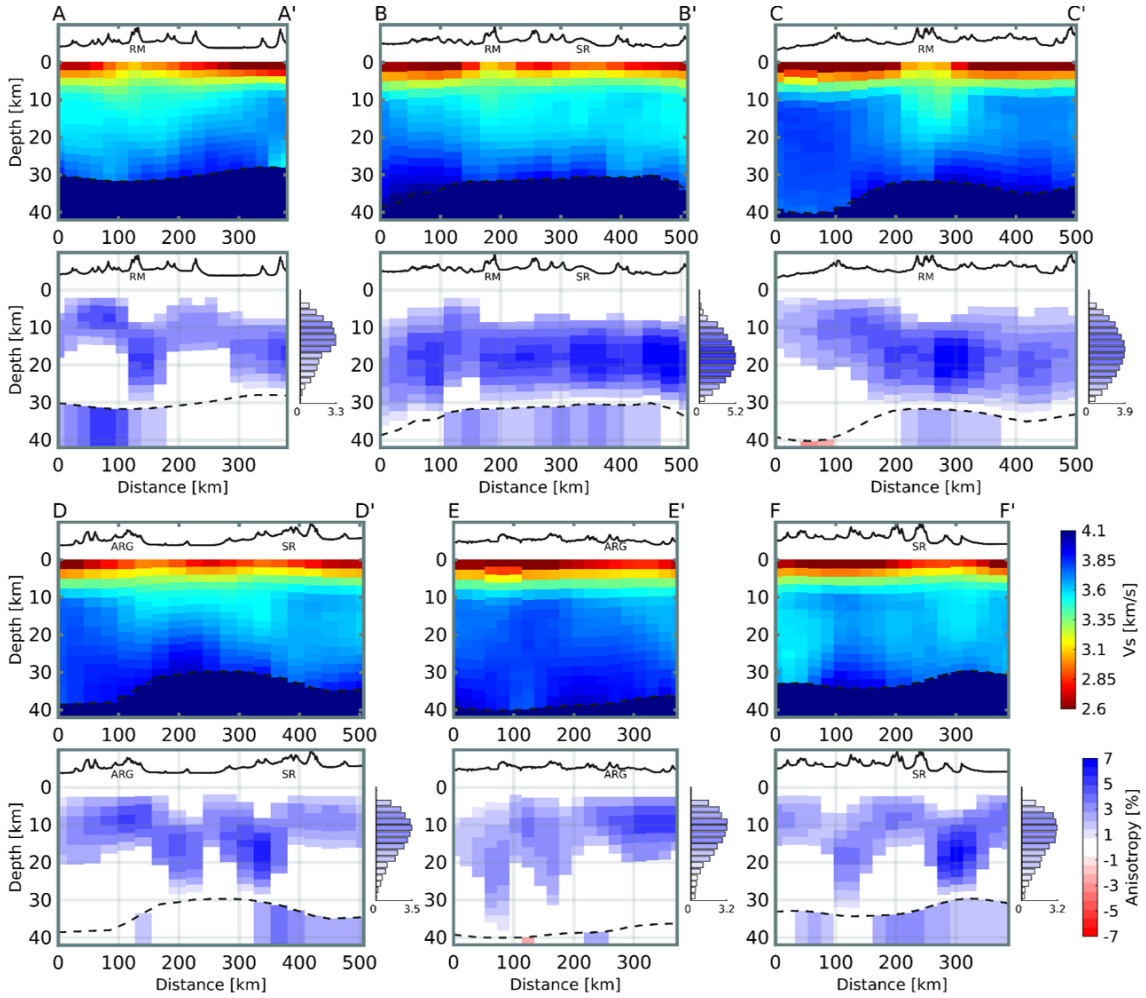

Figure S10. Same as figure 8, but showing only isotropic V_S and anisotropy cross sectional (see figure 1) results from inversion case 5 that have an absolute value of radial anisotropy with a significance greater than one standard deviation of the posterior distribution. Bar charts right of anisotropy cross-sections show average anisotropy profiles with depth for each cross-section. Anisotropy minima and maxima are labeled on the x-axis of each profile and colors correspond to anisotropy color bar. All panels shown here use the crustal thickness (dashed line) model of Schmandt et al., (2015). Topography is exaggerated 3 times in the profiles at the top of each panel.

Seismic network	DOI
TA	https://doi.org/10.7914/SN/TA
YX (RMSE)	https://doi.org/10.7914/SN/YX_2010
BK	https://doi.org/10.7932/BDSN
CI	https://doi.org/10.7914/SN/CI
IW	https://doi.org/10.7914/SN/IW
LB	N/A- http://www.fdsn.org/networks/detail/LB/
US	https://doi.org/10.7914/SN/US
UU	https://doi.org/10.7914/SN/UU

Table S1. Summary of seismic networks used for this study.

Period	Rayleigh error	Love Error
5	.050	-
6	.045	.040
8	.044	.035
10	.043	.033
12	.038	.032
15	.037	.032
20	.038	.033
25	.039	.032
30	.036	.029

Table S2. Rayleigh and Love wave errors at periods 5-30 s following Jiang et al., (2018).